Shear wave speed recovery using moving interference patterns obtained in sonoelastography experiments

Joyce McLaughlin and Daniel Renzi[a)]
Mathematics Department, Rensselaer Polytechnic Institute, Troy, New York 12180

Kevin Parker
ECE Department, University of Rochester, Rochester, New York 14627

Zhe Wu
GE Healthcare, Milwaukee, Wisconsin 53201

(Received 17 November 2005; revised 4 December 2006; accepted 6 January 2007)

Two new experiments were created to characterize the elasticity of soft tissue using sonoelastography. In both experiments the spectral variance image displayed on a GE LOGIC 700 ultrasound machine shows a moving interference pattern that travels at a very small fraction of the shear wave speed. The goal of this paper is to devise and test algorithms to calculate the speed of the moving interference pattern using the arrival times of these same patterns. A geometric optics expansion is used to obtain Eikonal equations relating the moving interference pattern arrival times to the moving interference pattern speed and then to the shear wave speed. A cross-correlation procedure is employed to find the arrival times; and an inverse Eikonal solver called the *level curve method* computes the speed of the interference pattern. The algorithm is tested on data from a phantom experiment performed at the University of Rochester Center for Biomedical Ultrasound.
 [DOI: 10.1121/1.2534717]

PACS number(s): 43.80.Qf, 43.20.Jr [FD] Pages: 2438–2446

I. INTRODUCTION

The target in this paper is to produce an image of tissue where the imaging functional is a measure of shear stiffness. This problem has been addressed for over 10 years and is motivated by the fact that shear stiffness is the tissue elastic property that is felt in a palpation exam. Three types of experiments have emerged.

(a) Static experiment: The tissue is compressed (Konofagou *et al.*, 1998, 2000a, b; Konofagou, 2000; Ophir *et al.* 1991).
(b) Transient experiments: (1) A wave is initiated with a line source on the boundary, (Bercoff *et al.*, 2001; Catheline *et al.*, 1999; Gennisson *et al.* 2003; Sandrin *et al.*, 2001, 2002a, b; Tanter *et al.* 2003), or in the interior (Bercoff *et al.*, 2002, 2004), and a wave with a front propagates away from the source; (2) a wave is initiated at a point (Nightingale *et al.* 2002, 2003), and propagates away from the source; and (3) a traveling wave is produced by harmonic excitation at two different points, each excited at two different but nearby frequencies (Wu *et al.*, 2004, 2006).
(c) Dynamic excitation: (1) A time harmonic excitation made on the boundary creates a time harmonic wave in the tissue (Lerner *et al.*, 1988; Gao *et al.*, 1995; Levinson and Sata, 1995; Taylor *et al.*, 2000; Manduca *et al.*, 2001; Wu *et al.*, 2002); and (2) a time harmonic excitation in the interior (Greenleaf and Fatemi, 1998) creates a time harmonic radiating wave.

For most of these experiments interior displacement on a fine grid of points in an imaging plane is measured with ultrasound or magnetic resonance and the excitation is low frequency (50–200 Hz); in Greenleaf and Fatemi (1998). an interior point source excitation at a few kilohertz yields a radiating wave which is measured on the surface of the body.

In McLaughlin and Renzi (2006a, b) the authors developed the Arrival Time algorithm for the transient elastography experiment developed in the laboratory of Fink (Catheline *et al.*, 1999; Sandrin *et al.*, 2002a, b). Important features in this work are: (1) A line source, with central frequency (50–200 Hz), initiates a shear wave with a front propagating in the interior; (2) the ultrafast imaging system developed by Fink *et al.* has a frame rate of up to 10 000 frames/s enabling identification of the wave front and its arrival time on a sufficiently fine grid in the image plane; and (3) the Arrival Time algorithm recovers the shear stiffness in the imaging plane from the space/time position of the wave front.

In this paper we focus on the application of the Arrival Time algorithm to image shear stiffness using data from two new sonoelasticity experiments developed by Wu and Parker at the University of Rochester. The key feature of these experiments is that the display of the Doppler spectral variance on a GE LOGIC 700 Doppler ultrasound machine shows a very slow moving traveling wave.

In the crawling wave experiment (Wu *et al.* 2004, 2006), two time harmonic excitations at nearby but not equal frequencies, are created on opposite sides of the tissue. In the holographic wave experiment (Wu *et al.* 2006), one time harmonic excitation is made in the tissue, and a second os-

[a)]Author to whom correspondence should be addressed; Electronic mail: renzid@rpi.edu

cillation at a nearby but not equal frequency is made in the ultrasound transducer where a gel is applied so that no resultant wave propagates into the tissue.

The common features of the two experiments are: (1) The GE LOGIC 700 display shows the radial component of a slowly moving interference pattern which would be stationary if the frequencies were the same; (2) the speed of the interference pattern is a small fraction of the shear wave speed; and (3) a Doppler ultrasound scanner samples the very slowly moving interference pattern effectively at a frame rate similar to the ultrafast imaging system frame rate for a wave moving at the shear wave speed. The main differences of the two experiments are: (1) The crawling wave interference display is governed by the sum of the two waves generated by the sources; and the holographic wave display is governed by the relative motion of the tissue oscillation and the transducer oscillation; (2) the interference pattern for the crawling wave has nearly parallel interference maxima; and for the holographic wave the interference patterns are more circular; (3) the amplitude of the holographic wave decreases with distance from the source; and the amplitude of the crawling wave is more uniform; (4) for the holographic wave the speed of the moving interference pattern is directly proportional to the shear wave speed; and for the crawling wave the relationship between the speed of the interference pattern and the shear wave speed is quite complicated in inhomogeneous regions; see Sec. IV; and (5) an advantage of the holographic wave experiment is that the tissue need only be accessible for excitation in one location.

To create our images we treat a stripe in a moving interference pattern as a wave packet and then: (a) Identify the arrival time of the wave packet at each point in the image plane; (b) find the Eikonal equation satisfied by this arrival time; and (c) apply the *level curve method* for the Arrival Time algorithm (McLaughlin and Renzi, 2006b) to the Eikonal equation to solve an inverse problem and image stiffness. Prior to this work, Wu *et al.* (2004) used the distance between interference maxima in the crawling wave experiment in a homogeneous phantom to determine the constant speed. This method, called the low frequency estimation method, is also applied to both experiments performed on a phantom with inclusion in Wu *et al.* (2006). In the current paper, the image of the inclusion is significantly improved when the image is created with the Arrival Time algorithm. Furthermore, the Arrival Time algorithm is fully two dimensional, taking into consideration the depth and transverse spreading of the lines of constant phase.

The rest of this paper is composed as follows: The experimental setups for each experiment are illustrated in Sec. II. Next, the mathematical model for each experiment is given in Sec. III. The equations relating the moving interference pattern speed and the shear wave speed are derived in Sec. IV. Two subalgorithms needed to create the shear stiffness images are explained in Secs. V and VI. Section VII contains reconstructions of a heterogeneous phantom with data from both experiments. Concluding remarks are given in Sec. VIII.

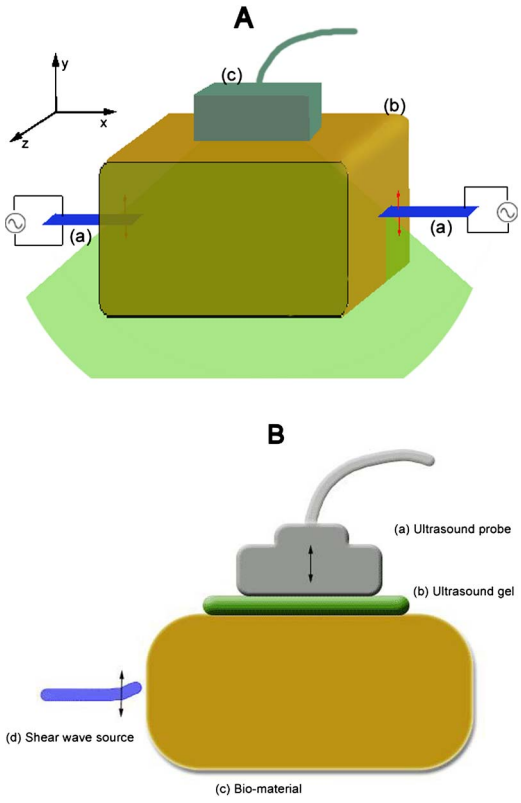

FIG. 1. (Color online) (A) Setup of the crawling wave experiment. Here the shear wave vibration sources are at (a), and the biomaterial and ultrasound probe are at (b) and (c) respectively. (B) Setup of the holographic wave experiment. Figure taken from Wu *et al.* (2006).

II. EXPERIMENTAL SETUPS AND THE DATA

The experimental apparatus for the crawling and holographic wave experiments are shown in Figs. 1(A) and 1(B). The GE LOGIC 700 Doppler ultrasound machine presents a 4 bit display of the Doppler spectral variance which is a good estimation of vibration amplitude (Wu *et al.*, 2004) and therefore displays a wave slowly moving across the screen. The Doppler spectral variance is the square of the sum of the excitations in the crawling wave experiment or the square of the difference in the excitations in the holographic wave experiment under some assumptions explained in the following.

For the crawling wave experiment we represent the radial components of the wave from each source as $A_r \sin(\omega_1 t - \omega_1 \phi_1)$, $B_r \sin(\omega_2 t + \omega_2 \phi_2)$. The backscattered ultrasound signal (see Huang *et al.*, 1990) can be represented as

$$s(t) = \cos\left(\omega_0 t + \frac{4\pi}{\lambda_0}(A_r \sin(\omega_1(t-\phi_1)) + B_r \sin(\omega_2(t+\phi_2)))\right)$$

where ω_0 is the ultrasound frequency and λ_0 is the wavelength of the ultrasound wave. Using basic trigonometry we can rewrite $s(t)$ as

$$s(t) = \cos\Big(\omega_0 t + \frac{4\pi}{\lambda_0} G \sin(t(\omega_1+\omega_2)/2 - (\omega_1\phi_1 - \omega_2\phi_2)/2 + \alpha)\Big),$$

where

$$G = [(A_r + B_r)^2 \cos^2(t(\omega_1-\omega_2)/2 - (\omega_1\phi_1 + \omega_2\phi_2)/2) + (A_r - B_r)^2 \sin^2(t(\omega_1-\omega_2)/2 - (\omega_1\phi_1+\omega_2\phi_2)/2)]^{1/2}$$

and

$$\alpha = \tan^{-1}\left[\left(\frac{A_r - B_r}{A_r + B_r}\right)\tan(t(\omega_1-\omega_2)/2 - (\omega_1\phi_1+\omega_2\phi_2)/2)\right].$$

In our examples $\omega_1-\omega_2 \sim 0.1$ Hz and $\omega_1+\omega_2 \sim 400$ Hz, so G and α are slowly varying and can be considered as stationary during the time interval for calculating the spectral variance. The Doppler spectral variance is then proportional to G^2 which is, again using basic trigonometry, with $\psi(\boldsymbol{x},t) = t(\omega_1-\omega_2) - (\omega_1\phi_1+\omega_2\phi_2)$,

$$G^2 = A_r^2 + B_r^2 + 2A_rB_r \cos\psi(\boldsymbol{x},t). \tag{1}$$

For the holographic wave experiment let $B\sin(\omega_2 t)$ be the vibration of the ultrasound transducers; the backscattered signal is the vibration of the tissue relative to the vibration in the transducer, so

$$s(t) = \cos\Big(\omega_0 t + \frac{4\pi}{\lambda_0}(A_r \sin(\omega_1 t - \phi_1) - B\sin(\omega_2 t))\Big) = \cos\Big(\omega_0 t + \frac{4\pi}{\lambda_0}\tilde{G}\sin(t(\omega_1+\omega_2)/2 - \omega_1\phi_1/2 + \tilde{\alpha})\Big)$$

where

$$\tilde{\alpha} = \tan^{-1}\left[\frac{A_r + B}{A_r - B}\tan^{-1}(t(\omega_1-\omega_2)/2 - \omega_1\phi_1/2)\right].$$

Here the displayed quantity is

$$\tilde{G}^2 = A_r^2 + B^2 - 2A_rB\cos\psi(\boldsymbol{x},t), \tag{2}$$

where now $\phi_2 = 0$ and so $\psi(x,t) = t(\omega_1-\omega_2) - \omega_1\phi_1$.

Both G^2 and $\tilde{G}^2$ can be rewritten as the amplitude of the sum (or difference) of the complexification of the induced vibrations

$$G^2 = |A_r e^{i\omega_1(t-\phi_1)} + B_r e^{i\omega_2(t-\phi_2)}|^2,$$

$$\tilde{G}^2 = |A_r e^{i\omega_1(t-\phi_1)} - Be^{i\omega_2 t}|^2.$$

These are the identities presented in Wu *et al.* (2006). Here we explain the assumptions under which they are obtained from the spectral variance.

III. MATHEMATICAL MODEL

Because stiffness is an elastic property and the displacements generated from the vibrators are small (on the order of microns), we use the linear elastic system of differential equations as our mathematical model. Assuming also that the medium is isotropic, the vector elastic displacement, $\boldsymbol{u}$, is then governed by the following system of equations:

$$(\lambda u_{j,j})_{,i} + (\mu(u_{i,j} + u_{j,i}))_{,j} - \rho u_{i,tt} = 0, \tag{3}$$

where λ, μ are the Lamé parameters and ρ is the density.

IV. EQUATIONS FOR THE IMAGING FUNCTIONALS

In the crawling wave experiments, the displacements $\boldsymbol{u}^1, \boldsymbol{u}^2$, from the first and second vibration sources, respectively, and $\boldsymbol{u} = \boldsymbol{u}^1 + \boldsymbol{u}^2$ all satisfy Eq. (3). The goal here is to find an equation for the phases for each of these quantities and then to derive a relationship between the phase $\psi(\boldsymbol{x},t) = t(\omega_1-\omega_2) - (\omega_1\phi_1+\omega_2\phi_2)$, or $\psi(\boldsymbol{x},t) = t(\omega_1-\omega_2) - \omega_1\phi_1$, seen in expressions (1) and (2), respectively, and the shear wave speed.

To accomplish this goal we first assume that $\boldsymbol{u}, \boldsymbol{u}_1, \boldsymbol{u}_2$ represent the complexification of the corresponding displacements. We use the geometric optics approximation (Ji *et al.* 2003; Ji and McLaughlin, 2004) for $\boldsymbol{u}^1$,

$$\boldsymbol{u}^1(\boldsymbol{x},t) = \boldsymbol{A}e^{i\omega_1(t-\phi_1)}, \tag{4}$$

where $\boldsymbol{A}$ is represented by the asymptotic expansion, $\boldsymbol{A} = \boldsymbol{A}_0 + \boldsymbol{A}_1/(i\omega_1) + \boldsymbol{A}_2/(i\omega_1)^2 + \cdots$. Substituting this expansion into Eq. (3), writing the left-hand side of Eq. (3) in powers of ω_1, and setting the coefficient of the highest order terms of ω_1 equal to zero results in (see Ji and McLaughlin, 2004)

$$0 = M\boldsymbol{A}_0, \tag{5}$$

where M is the following matrix:

$$M = [(\lambda+\mu)\nabla\phi_1(\nabla\phi_1)^T + (\mu|\nabla\phi_1|^2 - \rho)I]. \tag{6}$$

The assumption here is that there is enough separation of scales so that the coefficient of each power of ω_1 is separately equal to zero. For Eq. (5) to have a solution, the matrix M must be singular. Setting the determinant of M equal to zero yields that either

$$|\nabla\phi_1(\boldsymbol{x})| = \sqrt{\rho/\mu} = 1/C_s, \tag{7}$$

or

$$|\nabla\phi_1(\boldsymbol{x})| = \sqrt{\rho/(\lambda+2\mu)} = 1/C_p, \tag{8}$$

where C_s and C_p are the shear and compression wave speeds, respectively. Equations (7) and (8) are called Eikonal equations. In soft tissue, λ is several orders of magnitude greater than μ (Sarvazyan *et al.*, 1995). Furthermore, for the constant coefficient case in an elastic half space, the exact solution of Eq. (3) has been found in Miller and Pursey (1954) and from this solution it is clear that the amplitude of the compression wave is very small, $O((\mu/\lambda)^2)$, when the ratio λ/μ is large. For this reason we will assume that Eq. (7) is satisfied. Likewise, we write the displacement, $\boldsymbol{u}^2$, from the second source as

$$\boldsymbol{u}^2(\boldsymbol{x},t) = \boldsymbol{B}e^{i\omega_2(t-\phi_2(t))} \tag{9}$$

and as above, the phase, ϕ_2, satisfies

$$|\nabla\phi_2(\boldsymbol{x})| = \sqrt{\rho/\mu} = 1/C_s. \tag{10}$$

To obtain the equation for ψ we use the idea that ψ and the speed, F, of the moving interference pattern in the direction $-\nabla\psi$ satisfy the Eikonal equation $|\nabla\psi(\boldsymbol{x},t)|F(\boldsymbol{x})=\psi_t$. (See Osher and Sethian (1988); Sethian (1999); Osher and Fedkiw (2002), and Appendix A.)

In addition, because ψ_t is the constant $\Delta\omega=\omega_1-\omega_2$, only the spatially varying component of the phase, which is $\hat{\psi}(\boldsymbol{x})=\omega_1\phi_1+\omega_2\phi_2$ for the crawling wave and $\hat{\psi}(\boldsymbol{x})=\omega_1\phi_1$ for the holographic wave is present in the formula for the speed, F. So

$$F=\frac{\omega_1-\omega_2}{|\nabla\hat{\psi}(\boldsymbol{x})|}=\frac{\Delta\omega}{|\nabla\hat{\psi}(\boldsymbol{x})|}. \tag{11}$$

We use this equation and the Arrival Time algorithm to find F and use $\omega_1F/\Delta\omega$ and $2\omega_1F/\Delta\omega$ as our imaging functionals for the holographic wave and crawling wave experiments, respectively, as we explain below.

The speed F is a simple multiple of the shear wave speed in the holographic wave experiment but not for the crawling wave experiment. To show this we first calculate $|\nabla\hat{\psi}(\boldsymbol{x})|^2$ as

$$\begin{aligned}|\nabla\hat{\psi}(\boldsymbol{x})|^2&=|\omega_1\nabla\phi_1(\boldsymbol{x})+\omega_2\nabla\phi_2(\boldsymbol{x})|^2\\&=\omega_1^2|\nabla\phi_1(\boldsymbol{x})|^2+\omega_2^2|\nabla\phi_2(\boldsymbol{x})|^2\\&\quad+2\omega_1\omega_2\nabla\phi_1(\boldsymbol{x})\cdot\nabla\phi_2(\boldsymbol{x})\\&=\omega_1^2|\nabla\phi_1(\boldsymbol{x})|^2+\omega_2^2|\nabla\phi_2(\boldsymbol{x})|^2\\&\quad+2\omega_1\omega_2|\nabla\phi_1(\boldsymbol{x})||\nabla\phi_2(\boldsymbol{x})|\cos(\theta),\end{aligned} \tag{12}$$

where θ is the angle between $\nabla\phi_1(\boldsymbol{x})$ and $\nabla\phi_2(\boldsymbol{x})$. Now, for the holographic wave experiment $\phi_2=0$ and

$$\begin{aligned}F^2&=\frac{\Delta\omega^2}{|\nabla\hat{\psi}|^2}=\frac{\psi_t^2(\boldsymbol{x},t)}{|\nabla\psi(\boldsymbol{x},t)|^2}=\frac{\Delta\omega^2C_s^2}{(\omega_1^2)}\\&\Rightarrow F=\frac{\Delta\omega C_s}{\omega_1}\text{ or }C_s=\frac{\omega_1F}{\Delta\omega}.\end{aligned} \tag{13}$$

For the crawling wave experiment the relationship between the crawling wave speed, F, and the shear wave speed, C_s, is more complicated. Therefore, using Eqs. (7), (10), and (12) we have

$$|\nabla\hat{\psi}(\boldsymbol{x})|^2=(1/C_s^2)(\omega_1^2+\omega_2^2+2\omega_1\omega_2\cos(\theta)). \tag{14}$$

Calculating the ratio $\psi_t^2/|\nabla\psi(\boldsymbol{x},t)|^2$ we obtain

$$\begin{aligned}F^2&=\frac{\Delta\omega^2}{|\nabla\hat{\psi}(\boldsymbol{x})|^2}=\frac{\psi_t^2}{|\nabla\psi|^2}\\&=\frac{\Delta\omega^2C_s^2}{2\omega_1^2(1+\cos(\theta))+O(\omega_1\Delta\omega_1)+O(\Delta\omega^2)}\end{aligned} \tag{15}$$

$$=\frac{\Delta\omega^2C_s^2}{4\omega_1^2\cos^2(\theta/2)+O(\omega_1\Delta\omega_1)+O(\Delta\omega^2)}. \tag{16}$$

This equation cannot be used to directly find the wave speed, $C_s(\boldsymbol{x})$, from the phase, $\psi(\boldsymbol{x},t)$, because in the inhomogeneous medium case the $\cos(\theta/2)$ term depends on the unknowns $\phi_1(\boldsymbol{x})$ and $\phi_2(\boldsymbol{x})$. However, Eqs. (7), (10), and (15) are a coupled system of three equations that can be solved for C_s, $\phi_1(\boldsymbol{x})$, and $\phi_2(\boldsymbol{x})$. This will be the subject of a future paper. So here for the crawling wave experiment we do not image C_s but instead use the quantity $2\omega_1F/\Delta\omega$ as an imaging functional. Note that similar expressions relating phase wave speed to C_s are found in Wu *et al.* (2006), under a locally constant assumption and without showing the relationship to the underlying elastic equations.

Remark 1: We measure only one component of the vibration amplitude. This is not a restriction since all components of the vibrational amplitude have the same phase under the geometric optics assumption.

Remark 2: The vibration amplitude is measured in a plane. So, out-of-plane derivatives cannot be calculated and are assumed to be zero. If there is significant out-of-plane motion of the moving interference pattern, this assumption causes overestimation of the imaging functional.

Remark 3: For the holographic experiment the direction of propagation of the shear wave is $\nabla\hat{\psi}=\omega_1\nabla\phi_1/\Delta\omega$; so the moving interference pattern moves either in the same (if $\omega_1>\omega_2$) or directly opposite direction (if $\omega_1<\omega_2$) as the shear wave induced by the source vibrating in the phantom (or tissue). For the crawling wave experiment $\nabla\hat{\psi}=(\omega_1\nabla\phi_1+\omega_2\nabla\phi_2)/\Delta\omega$; so the direction of the moving interference pattern is not, in general, in the same direction as either of the shear waves induced individually by the two sources.

V. CALCULATING PHASE AND ARRIVAL TIME

To utilize $|\nabla\hat{\psi}|F=\Delta\omega$ we must first construct a continuously varying phase, $\hat{\psi}$, from the data, $|u_r|^2=A_r^2+B_r^2+2A_rB_r\cos(\Delta\omega t-\hat{\psi})$. This is related to the classic phase unwrapping problem.

Furthermore, we can interpret a multiple of $\hat{\psi}$ as an arrival time. This is based on the observation that at an arbitrary fixed point, $\boldsymbol{x}_0$, the time trace of the data can be represented by a constant plus $2(A_rB_r)(\boldsymbol{x})\cos((\omega_2-\omega_1)t-\hat{\psi}(\boldsymbol{x}))$. After filtering out the constant, consider the time trace $V(\boldsymbol{x}_0,t)=2(A_rB_r(\boldsymbol{x}_0))\cos((\omega_1-\omega_2)t-\hat{\psi}(\boldsymbol{x}_0))$; an example of this is shown in Fig. 2(A) with a solid line. Now consider the time trace at a second fixed point, $\boldsymbol{x}_1$, with the additive constant also removed, $V(\boldsymbol{x}_1,t)=2(A_rB_r)(\boldsymbol{x}_1)(\cos((\omega_1-\omega_2)t-\hat{\psi}(\boldsymbol{x}_1)))$; see the dotted line in Fig. 2(A). Notice that, except for magnitude, $V(\boldsymbol{x}_1,t)$ is very nearly $V(\boldsymbol{x}_0,t)$ except that it is time delayed by $(\hat{\psi}(\boldsymbol{x}_1)-\hat{\psi}(\boldsymbol{x}_0))/\Delta\omega$. That is $(\omega_1-\omega_2)t-\hat{\psi}(\boldsymbol{x}_0)=(\omega_1-\omega_2)(t+\delta)t-\hat{\psi}(\boldsymbol{x}_1)$, and we can interpret $\hat{\psi}(\boldsymbol{x}_1)-\hat{\psi}(\boldsymbol{x}_0)$ as a scaled time delay. So it is appropriate to define the quantity $\hat{\psi}(\boldsymbol{x}_1)/\Delta\omega=T(\boldsymbol{x}_1)$ as the arrival time, of the signal $V(\boldsymbol{x}_0,t)$ at the point $\boldsymbol{x}_1$. With this in mind, for the rest of this paper, we will refer to the scaled phase $\hat{\psi}(\boldsymbol{x})/\Delta\omega$ as the arrival time, $T(\boldsymbol{x})$.

We compute the arrival time using

$$C(\boldsymbol{x},\delta t):=\frac{1}{T}\int_0^T\tilde{v}(\boldsymbol{x}_0,t)\tilde{v}(\boldsymbol{x},t+\delta t)dt,$$

where

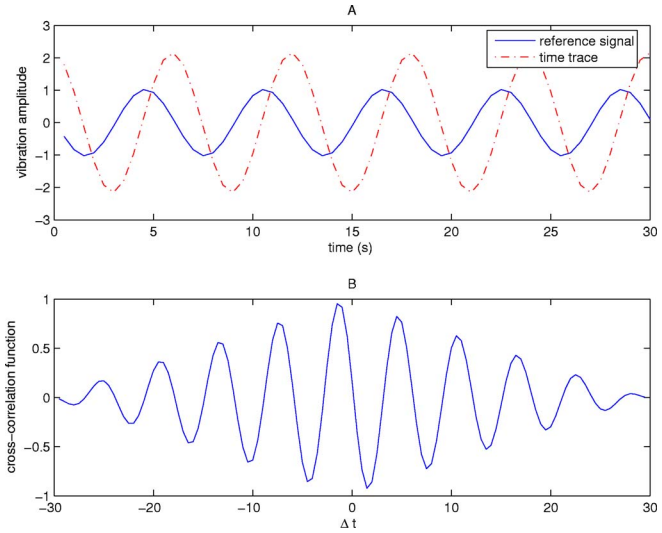

FIG. 2. (Color online) (A) Time traces of vibrational amplitude $V(\boldsymbol{x}_0,t)$ (solid line) and $V(\boldsymbol{x}_1,t)$ (dashed line). (B) Cross-correlation function of the two signals, $\tilde{v}(\boldsymbol{x}_1,t)$ and $\tilde{v}(\boldsymbol{x}_0,t)$.

$$\tilde{v}(\boldsymbol{x},t)=\begin{cases} V(\boldsymbol{x},t) & \text{if } 0\le t\le \hat{T} \\ V(\boldsymbol{x},t-\hat{T}) & \text{if } t>\hat{T} \\ V(\boldsymbol{x},t+\hat{T}) & \text{if } t>0. \end{cases}$$

See Fig. 2(B). Now we estimate the arrival times by $T(\boldsymbol{x}) \approx \delta t_{\max}$, where

$$\delta t_{\max} := \operatorname{argmax}_{\delta t\in[0,\hat{T}]} C(\boldsymbol{x},\delta t).$$

That is, δt, maximizes the correlation between the signals $\tilde{v}(\boldsymbol{x}_0,t)$ and $\tilde{v}(\boldsymbol{x},t+\delta t)$. To eliminate nonuniqueness that occurs because the two signals are cyclical, we: (1) Choose one of the maximums arbitrarily for the first point, $\boldsymbol{x}_0$; then, (2) for points neighboring $\boldsymbol{x}_0$, we choose local maxima in the cross-correlation function near the value $T(\boldsymbol{x}_0)$; and (3) to add stability to our procedure when finding the arrival time, $T(\boldsymbol{x})$, at a new point, $\boldsymbol{x}$, we use the median value of T at nearby points, that already have a computed arrival time, as a starting point.

We will use these computed arrival times as input to an inverse Eikonal solver described in the following; see also Ji *et al.* (2003); McLaughlin and Renzi (2006a, b). The output of this solver will be the speed of the moving interference pattern.

VI. SOLVING THE INVERSE EIKONAL EQUATION

The quantities $2\omega_1 F/\Delta\omega$ and $\omega_1 F/\Delta\omega$ are our imaging functionals for the crawling and holographic wave experiments, respectively. The goal now is to calculate $F=|\nabla T|^{-1}$ in a smart way, avoiding the essentially unstable calculation of dividing by derivatives of noisy data.

A slow, but robust, second-order method approximates the speed of the moving interference pattern using the elementary idea that speed is distance divided by time. So,

$$F \approx \left\{ \frac{1}{2\Delta t}\left(\min_{\hat{x}^+}|\boldsymbol{x}-\hat{\boldsymbol{x}}^+| + \min_{\hat{x}^-}|\boldsymbol{x}-\hat{\boldsymbol{x}}^-|\right) : \hat{\boldsymbol{x}}^{\pm} \text{ satisfies } T(\hat{\boldsymbol{x}}^{\pm}) = T(\boldsymbol{x}) \pm \Delta t \right\}. \quad (17)$$

We call this method for finding F the *distance method*. This is justified in McLaughlin and Renzi (2006a). A faster $0(m\log m)$ algorithm is described below.

Starting with the surface $S_T=\{(\boldsymbol{x},t)\,|\,T(\boldsymbol{x})=t, 0<t<T, \boldsymbol{x}\in\Omega\}$ where Ω is the image plane, define the higher dimensional function

$$\gamma(\boldsymbol{x},t) = \pm \min_{\hat{x}^+}\{|\boldsymbol{x}-\hat{\boldsymbol{x}}| : \hat{\boldsymbol{x}} \text{ satisfies } T(\boldsymbol{x})=t\}$$

where plus (minus) is chosen if $t>T(\boldsymbol{x})(t<T(\boldsymbol{x}))$, respectively. Then

$$\gamma(\boldsymbol{x},T(\boldsymbol{x}))=0 \text{ for } \boldsymbol{x}\in\Omega, \quad |\nabla\gamma|=1$$

so that

$$\gamma_t = |\nabla T|^{-1} = F \text{ on } \{(\boldsymbol{x},t)\,|\,\gamma(\boldsymbol{x},t)=0\} = S_T.$$

The potentially unstable term $|\nabla T|^{-1}$ is now replaced by γ_t which is in the numerator; and furthermore, no additional approximations are made to achieve this equation [see Osher and Fedkiw (2002); Sethian (1999), and Appendix A). For our inverse problem to obtain the $0(m\log m)$ algorithm speed, the extension from S_T to γ is made quickly and simultaneously for all times in our discretization. For those details, refer to McLaughlin and Renzi (2006b). The full algorithm for calculating the speed, F, in this way is called the *level curve method*. Note that as a final step we apply total variation minimization, (Rudin *et al.*, 1992).

VII. PHANTOM EXPERIMENTS

Combining the ideas from Sec. V (arrival time calculation) and Sec. VI (speed calculation from arrival times) gives a complete algorithm to recover interference pattern speed. The data are obtained using a Zerdine tissue mimicking phantom (CIRS Norfolk, VA), which is bowl-shaped and measures approximately $15\times15\times15$ cm in size. The phantom contains an isotropic background and a 1.3-cm-diam isotropic spherical stiff inclusion. The shear wave speed in the stiff inclusion is approximately $\sqrt{7}\approx2.65$ times faster than the background shear wave speed.

For the crawling wave experiment, two vibration sources are on opposite ends of the Phantom at frequencies, 250 and 250.15 Hz. Figure 3(A) shows a snapshot of the interference pattern in a middle region in the plane containing the two sources and the ultrasound transducer.

The first step to generate a shear wave speed reconstruction is to find the arrival times, T, from the spectral variance data. Before we do this, we preprocess the data. We use the one-dimensional fast Fourier transform on each time trace, and filter out all the frequencies except for a narrow band

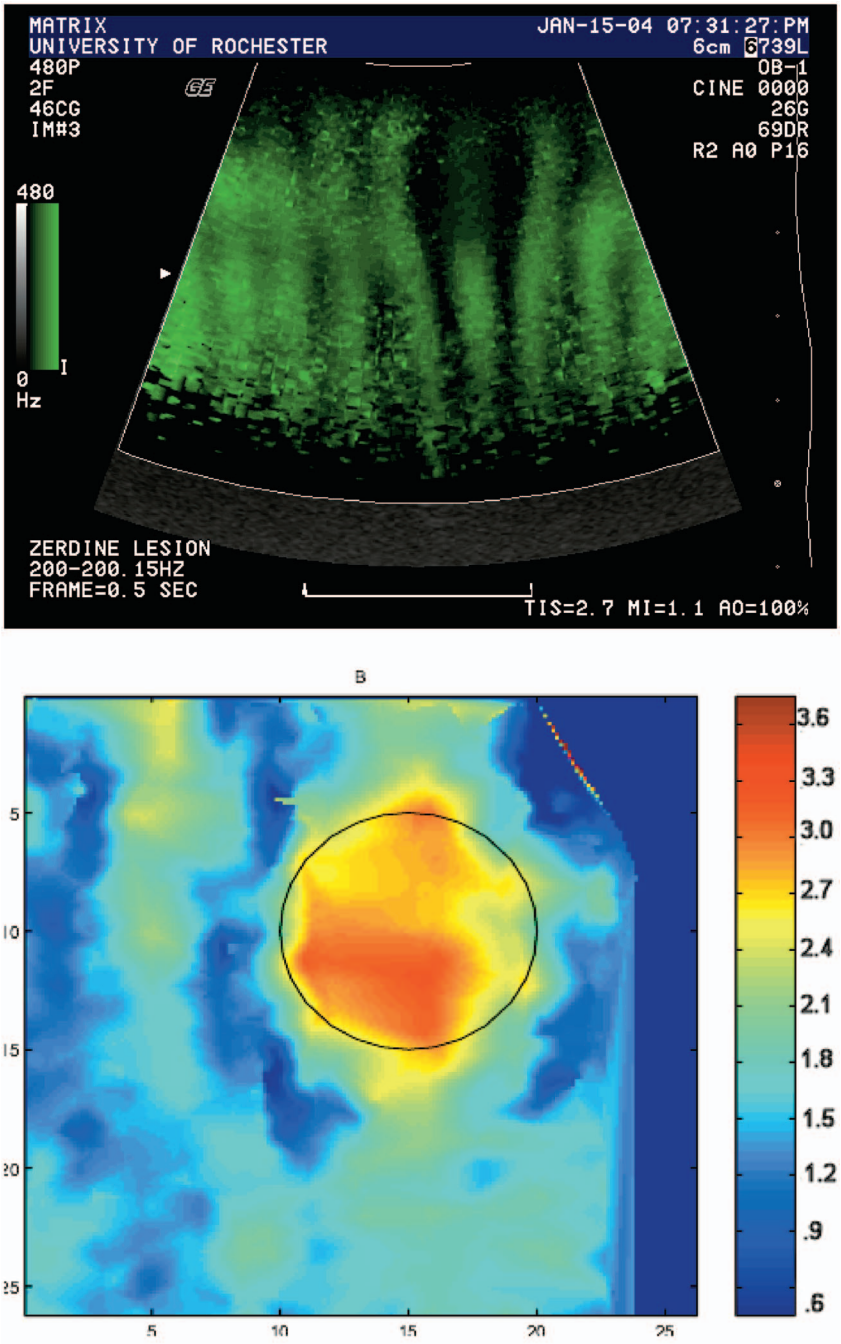

FIG. 3. (A) Snapshot of the moving interference pattern in the crawling wave experiment. (B) Imaging functional, $2\omega_1 F/\Delta\omega$, related to the shear wave speed in the crawling wave experiment. The units for the axis are millimeters and the color bar units are m/s.

around the driving frequency, $\Delta\omega=0.15$ Hz. Then we find the arrival time as discussed in Sec. VI. The interference pattern speed, $F=|\nabla T|^{-1}=\gamma_t$, is calculated with the inverse *level curve method* for the Arrival Time algorithm. The imaging functional, $2\omega_1 F/\Delta\omega$, is shown in Fig. 3(B). The wave speed contrast of the reconstruction is about 2.33, which is close to the actual wave speed contrast of 2.65. Note also the ring-like artifact around the recovered inclusion. This is likely due to the omission of the $\cos(\theta/2)$ term in our equation for the speed.

The interference patterns look very similar to a plane wave when two point sources are used. For an explanation, see Appendix B.

For the holographic wave experiment the frequency of the vibration source is 200.1 Hz. The ultrasound transducer is vibrated at 200 Hz. Figure 4(A) shows a snapshot of the moving interference pattern; it looks like an expanding half circle as one would expect from a point source. We find the arrival times, the interference pattern speed, F, as outlined in Secs. V and VI, and image the shear wave speed $C_s=\omega_1 F/\Delta\omega$; see Fig. 4(B). The imaging planes in the two experiments are at slightly different locations in the phantom. The black circle indicates the size of the stiff inclusion. In this reconstruction the wave speed contrast is almost 2, compared to the actual wave speed contrast of 2.65. There are fewer artifacts in this reconstruction. This is due to the more accurate relationship between the interference speed and the shear wave speed for the holographic wave experiment.

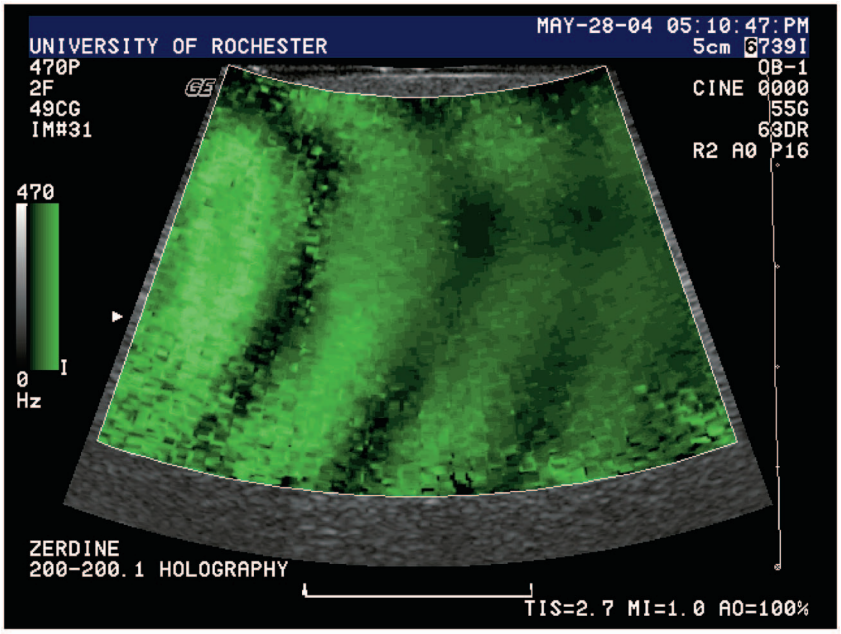

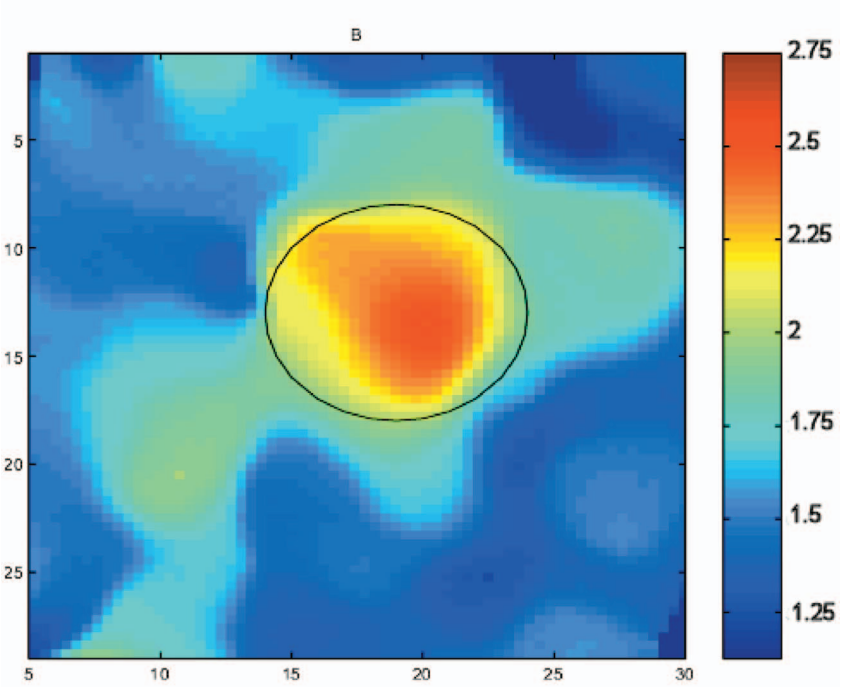

FIG. 4. (A) Snapshot of the moving interference pattern in the holographic wave experiment. (B) Recovery of the shear wave speed C_s in the holographic wave experiment. The units for the axis are millimeters and the color bar units are m/s.

VIII. SUMMARY AND CONCLUSION

We have developed a new algorithm, composed of two subalgorithms, to image the speed of moving interference patterns. The first subalgorithm finds the *arrival times* of one of the curves of interference maxima. The second subalgorithm takes as input the arrival times found by the first subalgorithm, and finds the moving interference pattern speed by solving the inverse Eikonal equation using the inverse *level curve method* for the Arrival Time algorithm. Our method is fully two dimensional taking into account both vertical and horizontal spread in the phase, and would easily generalize to three dimensions. The imaging functional is a multiple of the speed of the moving interference pattern.

There are two sources of artifacts in the images. One is the low bit rate achieved with only 16 levels of quantization in the display. We expect significantly less artifacts when the data gives a 256 color quantization. The second applies to the crawling wave experiment. Some artifacts occur because the imaging functional is a nonlinear function of the shear wave speed. These artifacts may be removed by solving the equations for ϕ_1, ϕ_2, and F simultaneously.

Note also, here we only consider interference pattern speed which is determined from the phase. When 256 color quantization data are available, one might consider also using a Helmholtz equation model, which has been considered in McLaughlin *et al.* (2006c); Dutt *et al.* (1997); Oliphant *et al.* (2000); Bishop *et al.* (2000); and Brown *et al.* (2001). Helmholtz inversion may be possible for the product $A\cos(\Delta\omega t - \omega_1\phi_1)$ obtained from the spectral variance calculation for the holographic wave experiment for experiments

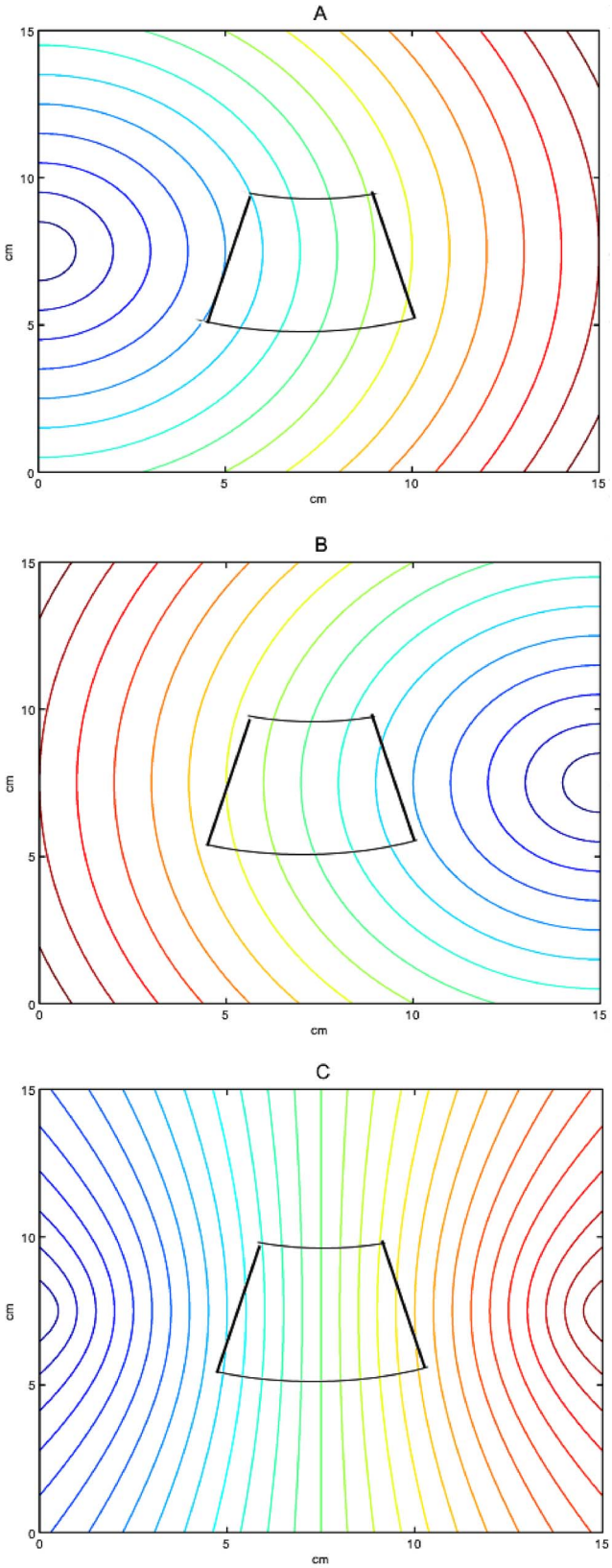

FIG. 5. (Color online) (A) Lines of constant phase for ϕ_1. (B) Lines of constant phase for ϕ_2. (C) Lines of constant phase for $\phi_1+\phi_2$. The solid black lines enclose the imaging region.

where: (1) There is very little out-of-of-plane motion; and (2) almost all excitation occurs in the radial direction (or downward direction if that is the direction of measurement). For the crawling wave experiment, this approach is more complicated since a differential equation that the expression $A_r B_r \cos(\Delta\omega t-(\omega_1\phi_1+\omega_2\phi_2))$ satisfies, even under the simplifying assumptions given earlier, is substantially more complicated.

It may, however, be possible to obtain a more accurate phase calculation by using the rf data more directly.

APPENDIX A

In this appendix we show that, on a level surface of the phase, $\psi(\boldsymbol{x},t)=k$,

$$\psi_t=|\nabla\psi|F \tag{A1}$$

is satisfied where F is the component of the velocity in the direction, $-\nabla\psi$, which is normal to the level curve $\psi(\boldsymbol{x},t)=k$, fixed k. Let $\boldsymbol{X}(t)$ be a parametric representation of a point lying on $\psi(\boldsymbol{x},t)=k$ with $x(t_0)=x_0$, some $(\boldsymbol{x}_0,t_0)$ satisfying $\psi(\boldsymbol{x}_0,t_0)=k$. Since $-\nabla\psi/|\nabla\psi|$ is normal to the curve $\psi(\boldsymbol{x},t_0)=k$, at $\boldsymbol{x}=\boldsymbol{x}_0$,

$$F(\boldsymbol{x}_0)=\boldsymbol{X}_t\cdot(-\nabla\psi/)|\nabla\psi|. \tag{A2}$$

Taking a time derivative of $\psi(\boldsymbol{x}(t),t)=k$ yields

$$\psi_t+\nabla\psi\cdot\boldsymbol{X}_t=0. \tag{A3}$$

Multiplying through Eq. (A3) by $1/|\nabla\psi|$, and using Eq. (A2), leads to

$$\psi_t=|\nabla\psi|F. \tag{A4}$$

Since $(\boldsymbol{x}_0,t_0)$ is arbitrarily chosen on $\psi(\boldsymbol{x},t)=k$, Eq. (A1) is established.

APPENDIX B

The interference pattern lines in Fig. 3 are similar to a plane wave for the following reasons: $\nabla\hat{\psi}/\Delta\omega\approx\omega_1(\nabla\phi_1+\nabla\phi_2)/\Delta\omega$ determines the direction of motion of the interference pattern; and (2) the image plane window is some distance from each source and the individual waves from each source move in opposite directions; this implies that in the background the vertical components of $\nabla\phi_1$ and $\nabla\phi_2$ will have opposite sign. To demonstrate we solve the equations $|\nabla\phi_1|=1$, and $-|\nabla\phi_2|=-1$, on a 15 cm$\times$15 cm square with the initial conditions $\phi_1(0,7.5)=0$, and $\phi_2(15,7.5)=0$. The lines of constant phase for ϕ_1 and ϕ_2 are simply expanding circles and are shown in Figs. 5(A) and 5(B). For $\phi_1+\phi_2$ the lines of constant phase, shown in Fig. 5(C), are given by a family of parabolas (Wu 2005). However, near the line equidistant to the two point sources the lines of constant phase for $\phi_1+\phi_2$ are nearly vertical; see Fig. 5(C). Note also that in Fig. 5(C) there are twice as many lines of constant phase as in Figs. 5(A) and 5(B). This is consistent with the additional factor of 2 in the crawling wave imaging functional.

Bercoff, J., Tanter, M., Chaffai, S., Sandrin, L., and Fink, M. (**2002**). "Ultrafast imaging of beam formed shear waves induced by the acoustic radiation force. Application to transient elastography," Proc.-IEEE Ultrason. Symp. **2**, 1899–1902.

Bercoff, J., Tanter, M., and Fink, M. (**2004**). "Supersonic shear imaging: A new technique for soft tissue elasticity mapping," IEEE Trans. Ultrason. Ferroelectr. Freq. Control **19**, 396–409.

Bercoff, J., Tanter, M., Sandrin, L., Catheline, S., and Fink, M. (**2001**). "Ultrafast compound imaging for 2D displacement vector measurements:

Application to transient elastography and color flow mapping," Proc.-IEEE Ultrason. Symp. **2**, 1619–1622.
Bishop, J., Samani, A., Sciaretta, J., and Plewes, D. B. (**2000**). "Two dimensional MR elastography with linear inversion reconstruction: Methodology and noise analysis," Phys. Med. Biol. **45**, 2081–2091.
Catheline, S., Thomas, J.-L., Wu, F., and Fink, M. (**1999**). "Diffraction field of a low frequency vibrator in soft tissues using transient elastography," IEEE Trans. Ultrason. Ferroelectr. Freq. Control **46**, 1013–1019.
Dutt, V., Manduca, A., Muthupillai, R., Ehman, R., and Greenleaf, J. (**1997**). "Inverse approach to elasticity reconstruction in shear wave imaging," Proc.-IEEE Ultrason. Symp. **2**, 1415–1418.
Gao, L., Parker, K. J., and Alam, S. K. (**1995**). "Sonoelasticity imaging: Theory and experimental verification," J. Acoust. Soc. Am. **97**, 3875–3880.
Gennisson, J. L., Catheline, S., Chaffai, S., and Fink, M. (**2003**). "Transient elastography in anisotropic medium: Application to the measurement of slow and fast shear wave speeds in muscles," J. Acoust. Soc. Am. **114**, 536–541.
Greenleaf, J. F., and Fatemi, M. (**1998**). "Ultrasound-stimulated vibroacoustic spectrography," Science **280**, 82–85.
Huang, S.-R., Lerner, R. M., and Parker, K. J. (**1990**). "On estimating the amplitude of harmonic vibration from the Doppler spectrum of reflected signals," J. Acoust. Soc. Am. **88**, 2702–2712.
Ji, L., and McLaughlin, J. R. (**2003**). "Shear stiffness identification in biological tissues: The full elastic model" (unpublished).
Ji, L., and McLaughlin, J. R. (**2004**). "Recovery of the Lamé parameter μ in biological tissues," Inverse Probl. **20**, 1–24.
Ji, L., McLaughlin, J. R., Renzi, D., and Yoon, J.-R. (**2003**). "Interior elastodynamics inverse problems: Shear wave speed reconstruction in transient elastography," Inverse Probl. **19**, S1–29.
Konafagou, E. E. (**2000**). "Precision estimation and imaging of normal and shear components of the 3D strain tensor in elastography," Phys. Med. Biol. **45**, 1553–1563.
Konafagou, E. E., Harrigan, T., and Ophir, J. (**2000a**). "Shear strain estimation and lesion mobility assessment in elastography," Ultrasonics **38**, 400–404.
Konafagou, E. E., and Ophir, J. (**1998**). "A new elastographic method for estimation and imaging of lateral displacements, lateral strains, corrected axial strains and Poisson's ratios in tissues," Ultrasound Med. Biol. **24**, 1183–1199.
Konafagou, E. E., Varghesse, T., and Ophir, J. (**2000b**). "Theoretical bounds on the estimation of transverse displacement, transverse strain and Poisson's ratio in elastography," Ultrason. Imaging **22**, 153–177.
Lerner, R. M., Parker, K. J., Holen, J., Gramiak, R., and Waag, R. C. (**1988**). "Sono-elasticity: Medical elasticity images derived from ultrasound signals in mechanically vibrated targets," Acoust. Imaging **16**, 317–327.
Levinson, S. F. M., and Sata, T. (**1995**). "Sonoelastic determination of human skeletal-muscle elasticity," J. Biomech. **28**, 1145–1154.
Manduca, A., Oliphant, T. E., Dresner, M. A., Mahowald, J. L., Kruse, S. A., Amromin, E., Felmlee, J. P., Greenleaf, J. F., and Ehman, R. L. (**2001**). "Magnetic resonance elastography: Non-invasive mapping of tissue elasticity," Med. Image Anal **5**, 237–254.
McLaughlin, J. R., and Renzi, D. (**2006a**). "Shear wave speed recovery in transient elastography and supersonic imaging using propagating fronts," Inverse Probl. **22**, 681–706.
McLaughlin, J. R., and Renzi, D. (**2006b**). "Using level set based inversion of arrival times to recover shear wave speed in transient elastography and supersonic imaging," Inverse Probl. **22**, 706–725.
McLaughlin, J. R., Renzi, D., Yoon, J.-R., Ehman, R. L., and Manducca, A. (**2006c**). "Variance controlled shear stiffness images for MRE data," *IEEE International Symposium on Biomedical Imaging, Macro to Nano* p. 960–963.
Miller, G., and Pursey, H. (**1954**). "The field and radiation impedance of mechanical radiators on the free surface of a semi-infinite isotropic solid," Proc. R. Soc. London, Ser. A **223**, 521–544.
Nightingale, K., Mcaleavey, S., and Trahey, V. (**2003**). "Shear-wave generation using acoustic radiation force: In vivo and ex vivo results," Ultrasound Med. Biol. **29**, 1715–1723.
Nightingale, K., Stutz, D., Bentley, R., and Trahey, G. (**2002**). "Acoustic radiation force impulse imaging: Ex vivo and in vivo demonstration of transient shear wave propagation," IEEE International Symposium on Biomedical Imaging, Cat. No. 02EX608 528-8
Oliphant, T. E., Kinnick, R. R., Manduca, A., Ehman, R. L., and Greenleaf, J. F. (**2000**). "An error analysis of Helmholtz inversion for incompressible shear vibration elastography with application to filter-design for tissue characterization," *Ultrasonics Symposium, 2000 IEEE*, Vol. **2**, pp. 1795–1798.
Ophir, J., Cespedes, I., Ponnekanti, H., Yazdi, Y., and Li, X. (**1991**). "Elastography: A quantitative method for imaging the elasticity of biological tissues," Ultrason. Imaging **13**, 111–134.
Osher, S. J., and Fedkiw, R. (**2002**). *Level Set Methods and Dynamic Implicit Surfaces* (Springer, Berlin).
Osher, S. J., and Sethian, J. A. (**1988**). "Front propagation with curvature dependent speed: Algorithms based on Hamilton-Jacobi formulations," J. Comput. Phys. **79**, 12–49.
Rudin, L. I., Osher, S., and Fatemi, E. (**1992**). "Nonlinear total variation based noise removal algorithms," Physica D **60**, 259–268.
Sandrin, L., Tanter, M., Catheline, S., and Fink, M. (**2002a**). "Shear modulus imaging with 2-D transient elastography," IEEE Trans. Ultrason. Ferroelectr. Freq. Control **49**, 426–435.
Sandrin, L., Tanter, M., Catheline, S., and Fink, M. (**2002b**). "Time-resolved 2D pulsed elastography. Experiments on tissue-equivalent phantoms and breast in-vivo," Proc. SPIE **4325**, 120–126.
Sandrin, L., Tanter, M., Gennisson, J. L., Catheline, S., and Fink, M. (**2001**). "Shear elasticity probe for soft tissues with 1-D transient elastography," IEEE Trans. Ultrason. Ferroelectr. Freq. Control **49**, 436–446.
Sarvazyan, A. P., Skovoroda, A. R., Emalianov, S. Y., Fowlkes, L. B., Pipe, J. G., Adler, R. S., and Carson, P. L. (**1995**). "Biophysical bases of elasticity imaging," Acoust. Imaging **21**, 223–240.
Sethian, J. A. (**1999**). *Level Set Methods and Fast Marching Methods: Evolving Interfaces in Computational Geometry, Fluid Mechanics, Computer Vision, and Materials Science* (Cambridge University Press, Cambridge).
Tanter, M., Bercoff, J., Sandrin, L., and Fink, M. (**2002**). "Ultrafast compound imaging for 2-D motion vector estimation: Application to transient elastography," IEEE Trans. Ultrason. Ferroelectr. Freq. Control **49**, 1363–1374.
Taylor, L. S., Porter, B. C., Rubens, D. J., and Parker, K. J. (**2000**). "Three-dimensional sonoelastography: Principles and practices," Phys. Med. Biol. **45**, 1477–1494.
Wu, Z. (**2005**). "Shear wave interferometry and holography, an application of sonoelasticity," Ph.D. thesis, University of Rochester, Rochester, NY.
Wu, Z., Rubens, D. J., and Parker, K. J. (**2006**). "Sonoelastographic imaging of interference patterns for estimation of the shear velocity distribution in biomaterials," J. Acoust. Soc. Am. **120**, 535-545.
Wu, Z., Taylor, L. S., Rubens, D. J., and Parker, K. J. (**2002**). "Shear wave focusing for three-dimensional sonoelastography," J. Acoust. Soc. Am. **111**, 439–446.
Wu, Z., Taylor, L. S., Rubens, D. J., and Parker, K. J. (**2004**). "Sonoelastographic imaging of interference patterns for estimation of the shear velocity of homogeneous biomaterials," Phys. Med. Biol., **49**, 911–922.